



A Tibetan lake sediment record of Holocene Indian summer monsoon variability



Broxton W. Bird^{a,*}, Pratigya J. Polisar^b, Yanbin Lei^c, Lonnie G. Thompson^d, Tandong Yao^c, Bruce P. Finney^e, Daniel J. Bain^f, David P. Pompeani^f, Byron A. Steinman^g

^a Department of Earth Sciences, Indiana University–Purdue University, Indianapolis, IN 46208, USA

^b Lamont Doherty Earth Observatory, Columbia University, New York, NY 10964, USA

^c Key Laboratory of Tibetan Environment Changes and Land Surface Processes Institute of Tibetan Plateau Research, Chinese Academy of Sciences, Beijing 100085, China

^d Byrd Polar Research Center, The Ohio State University, Columbus, OH 43210, USA

^e Department of Biological Sciences, Idaho State University, Pocatello, ID 83209, USA

^f Department of Earth and Planetary Sciences, University of Pittsburgh, PA 15217, USA

^g Department of Meteorology and Earth and Environmental Systems Institute, Pennsylvania State University, University Park, PA 16802, USA

ARTICLE INFO

Article history:

Received 2 July 2013

Received in revised form 2 May 2014

Accepted 7 May 2014

Available online 29 May 2014

Editor: J. Lynch-Stieglitz

Keywords:

paleoclimate

global change

grain size

leaf wax hydrogen isotopes

lake levels

ABSTRACT

Sedimentological data and hydrogen isotopic measurements of leaf wax long-chain *n*-alkanes (δD_{wax}) from an alpine lake sediment archive on the southeastern Tibetan Plateau (Paru Co) provide a Holocene perspective of Indian summer monsoon (ISM) activity. The sedimentological data reflect variations in lake level and erosion related to local ISM rainfall over the Paru Co catchment, whereas δD_{wax} reflects integrated, synoptic-scale ISM dynamics. Our results indicate that maximum ISM rainfall occurred between 10.1 and \sim 5.2 ka, during which time there were five century-scale high and low lake stands. After 5.2 ka, the ISM trended toward drier conditions to the present, with the exception of a pluvial event centered at 0.9 ka. The Paru Co results share similarities with paleoclimate records from across the Tibetan Plateau, suggesting millennial-scale ISM dynamics were expressed coherently. These millennial variations largely track gradual decreases in orbital insolation, the southward migration of the Intertropical Convergence Zone (ITCZ), decreasing zonal Pacific sea surface temperature (SST) gradients and cooling surface air temperatures on the Tibetan Plateau. Centennial ISM and lake-level variability at Paru Co closely track reconstructed surface air temperatures on the Tibetan Plateau, but may also reflect Indian Ocean Dipole events, particularly during the early Holocene when ENSO variability was attenuated. Variations in the latitude of the ITCZ during the early and late Holocene also appear to have exerted an influence on centennial ISM rainfall.

© 2014 Elsevier B.V. All rights reserved.

1. Introduction

Considerable effort has been directed toward developing paleoclimate records from the Tibetan Plateau and surrounding region in order to improve our understanding of the Indian summer monsoon (ISM) system. Syntheses of these records, which include lake, bog and speleothem archives, suggest a relatively brief early Holocene maximum in ISM precipitation between 10 and 7 ka that was followed by generally dry conditions (An et al., 2000; He et al., 2004; Herzschuh, 2006; Zhang et al., 2011). Centennially resolved ISM records from the Tibetan Plateau suggest rapid rainfall reductions at 11.5 ka and between 5 and 4 ka (Morrill

et al., 2003) and a possible link between ISM rainfall, total solar irradiance and/or North Atlantic sea surface temperatures (Porter and Weijian, 2006; Cai et al., 2012). Recently published lake-level reconstructions from the Tibetan Plateau (Chen et al., 2013; Hudson and Quade, 2013; Dietze et al., 2013), generally support the idea of a wet early Holocene and dry late Holocene, but are lower resolution and hence details regarding the timing, duration and nature of higher-frequency Holocene ISM variability remains less well understood. Unraveling the expression of long-term and abrupt Holocene ISM variability and the responsible mechanisms is critical, however, because this system is the primary source of fresh water for more than 1 billion people in South Asia (Xu et al., 2008). Indeed, extremes in ISM rainfall of either sign pose a significant hydro-meteorological threat to the region with the potential for far reaching socioeconomic consequences (The World Bank, 2012).

* Corresponding author. Tel.: +1 (317) 274 7468

E-mail address: bwbird@iupui.edu (B.W. Bird).

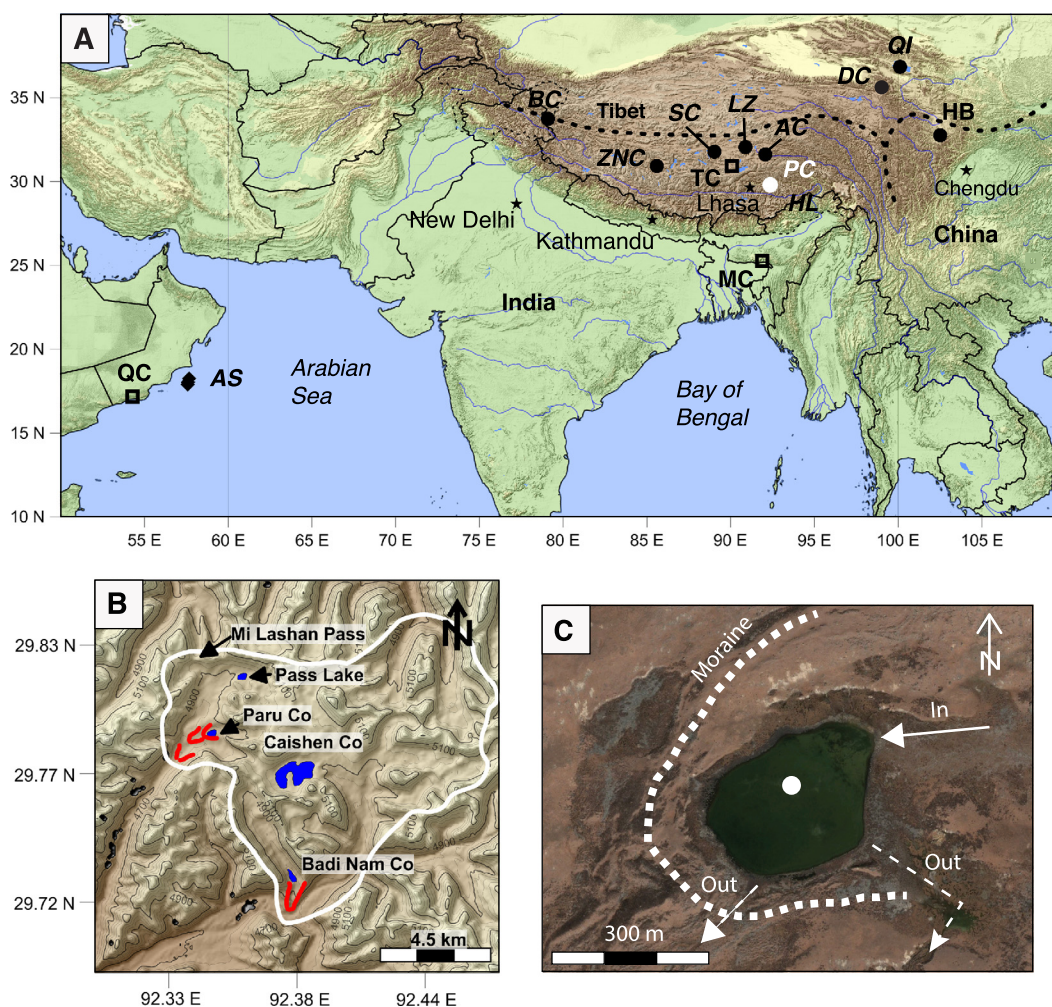


Fig. 1. (a) Map of southern Asia showing the location of sites mentioned in the text. Black dashed lines indicate the maximum extents of the Indian and Asian summer monsoons after Tian et al. (2007). Paru Co (PC), Hidden Lake (HL), Ahung Co (AC), Lake Zigetang (LZ), Tianmen Cave (TC), Seling Co (SC), Zhari Namco (ZNC), Bangong Co (BC), Qinghai (QI), Hongyuan Bog (HB), Mawmluh Cave (MC), Qunf Cave (QC) and the Arabian Sea sediment cores (AS). (b) Expanded view of the study area showing the location of Paru Co and other nearby lakes. Moraines are identified with red lines. The white line marks the approximate extent of the hypothesized ice cap that at one time may have covered the study area. (c) Satellite image of Paru Co and its immediate watershed, including the moraine dam (thick white dashed line), the core location (white circle), and the main location of seasonal inflow (solid white arrow) and the overflow point (dashed white arrow). (For interpretation of the references to color in this figure legend, the reader is referred to the web version of this article.)

Here we present an 11,000-yr record of ISM variability from Paru Co, a high-altitude lake on the southeastern Tibetan Plateau. Relative lake levels and local precipitation intensity are reconstructed with sedimentological proxies (e.g., grain size and lithic flux) at multi-decadal resolution, while hydrogen isotope ratios of terrestrial leaf waxes (δD_{wax}) are used to reconstruct the synoptic state of the ISM at millennial resolution. Combining these data sets, we investigate the timing, regional coherence and causes of Holocene ISM variability on the Tibetan Plateau.

2. Study site

Paru Co is a small (0.1 km²) moraine dammed lake in the Nyainqentanglha Mountains on the southeastern Tibetan Plateau at 4845 m above sea level (asl; Fig. 1; N29.796°, E92.352°). The lake's watershed (2.97 km²) consists of a broad, shallowly sloping glacial valley measuring 0.5 by 2.0 km with lateral mountain ridges of 5170 to 5140 m asl and a central ephemeral stream channel. The valley connects to a larger topographic plateau with extensive glacial landforms that lacks distinct cirques, suggesting an ice cap once covered the region (Fig. 1b). The plateau is currently unglaciated, and previous work in the region suggests that sites with headwalls below 5200 m asl were not glaciated during

the Holocene (Williams, 1983). The local bedrock is geologically homogeneous, consisting of Pleistocene age andesite (Choubert et al., 1983).

The modern lake is shallow with a maximum water depth of 1.2 m, with gently sloping sides and no permanent inflows or outflows. Seasonal runoff enters the lake on its northeastern shore with potential overflow accommodated by a low point in the moraine that is approximately 2 m higher than the current lake level (Fig. 1c). As a result, Paru Co could sustain a modern water level of approximately 3 m. An incised stream channel below the primary outlet indicates that the lake has overflowed at times in the past. A second incised, but currently dry, stream channel is located approximately 430 m west of the primary outlet, suggesting that this region may also accommodate overflow during exceptionally wet periods. Vegetation in the watershed and regionally is dominated by grasses with scattered pockets of shrubs (Tang et al., 2000).

Tropical Rainfall Measuring Mission data (TRMM) spanning 1998 to 2007 shows that 92 (86)% of mean annual precipitation (MAP; 1118 mm/yr) at Paru Co is delivered from April (May) through September during the ISM season (Fig. 2; Huffman et al., 2010). Sixty km west of Paru Co in Maizhokunggar (3895 m asl; 29.8296, 91.7470) MAP between 1991 and 2010 was 479 mm/yr,

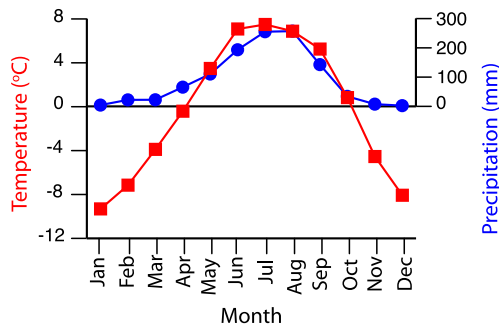


Fig. 2. (a) Average monthly precipitation at Paru Co based on TRMM data from 1998 to 2007. (b) Average monthly temperatures at Paru Co (4845 m asl) extrapolated from Lhasa (3650 m asl) weather station data using a lapse rate of $-6.4^{\circ}\text{C km}^{-1}$.

92% of which occurred between May and September. Higher TRMM precipitation may reflect elevation differences between the sites and/or calibration effects. Temperatures rise above 0°C from May through October, peaking in June and July (Fig. 2; Peterson and Vose, 1997). Below freezing temperatures and minimal precipitation occur for the rest of the year, resulting in cold dry conditions and seasonal ice cover over the lake.

3. Materials and methods

3.1. Sediment core and sample collection

Sediment cores, water, soil and vegetation were collected at Paru Co in May of 2011. A 60 cm surface core was retrieved using a percussion coring system and extruded in the field at 0.5 cm intervals from 0 to 10 cm and 1 cm intervals from 10 to 60 cm. A 435 cm sediment core was collected from Paru Co using a modified piston corer (Wright et al., 1984). Sequential 1 m drives were overlapped by 30 cm to ensure complete sediment recovery. The composite core was constructed by visually correlating stratigraphic units.

3.2. Initial core description, bulk density and loss on ignition

Sediment cores were split, photographed, described and volumetrically subsampled (1 cm^{-3}) at 2 cm intervals. Wet samples were weighed, dried for 24 h at 60°C and reweighed to determine dry bulk density (ρ_{dry} ; g cm^{-3}). Percent total organic matter (%TOM) and total carbonate (%TC) were then determined by weight loss after ignition at 550°C (4 h) and 1000°C (2 h), respectively (modified from Heiri et al., 2001).

3.3. Grain size

Approximately 1.0 g of wet sediment was collected at 1 cm intervals, dried for 24 h at 60°C and weighed. Samples were soaked in a 50 ml aliquot of 35% H_2O_2 at room temperature for 24 h and treated with five 20 ml aliquots of 35% H_2O_2 at 65°C to remove organic matter (Gray et al., 2010). Biogenic silica was removed with a 20 ml 1N NaOH digestion (8 hr at 60°C) and verified by smear slide for 10% of the samples. Acid washing was not performed because no carbonate was present. Treated samples were freeze dried and weighed to calculate the lithic abundance (%Lithics). Grain size measurements were performed on the lithic fraction using a Malvern Mastersizer 2000 with reported values calculated using the average of three replicate measurements.

3.4. Biogenic silica

Biogenic silica abundances (%BSi) were estimated using the equation: $100\% - \%OM - \%TC - \%Lithics = \%Residual$, assuming that

%Residual reflects %BSi. Biogenic silica was also determined analytically on a subset of 46 samples using a wet-alkali dissolution method (0.1 M Na_2CO_3 at 85°C for 5 hr) modified from Mortlock and Froelich (1989) and measured by molybdate-blue spectrophotometry. Values are reported as 10% hydrated silica ($\text{SiO}_2 \cdot 0.4\text{H}_2\text{O}$) using a multiplier of 2.4 times the weight percent of biogenic silica content (Mortlock and Froelich, 1989). An estimated error of $<4.6\%$ (calculated as the coefficient of variation) is based on replicate measurements of two internal sediment standards.

3.5. Long-chain *n*-alkane (leaf wax) hydrogen isotopes

Total lipids were extracted (TLE) from freeze dried samples with a Dionex ASE-350 using 9:1 dichloromethane:methanol (v/v). The TLE was separated with a silica gel column (0.5 g, 70–230 mesh, 60 Å pore size) by elution with 4 ml each of hexane (aliphatic), dichloromethane (ketone/ester) and methanol (acid/polar). Saturated compounds were purified from the aliphatic fraction by chromatography over silver-impregnated silica gel (0.5 g of 10% w/w AgNO_3 on silica gel, Sigma-Aldrich) with hexane (4 ml). *n*-Alkane hydrogen isotopes were measured with a Thermo Trace gas chromatograph coupled through a high-temperature pyrolysis reactor to a Thermo Delta V mass spectrometer. Measurements were referenced to the VSMOW scale using mixtures of 15 *n*-alkanes (Mix A5) with isotopic compositions determined by offline reduction by Arndt Schimmelmann (University of Indiana). Analytical uncertainty of reported values is 3.4 to 4.5‰ (1σ s.e.m.), incorporating uncertainty of replicate analyses and realization of the VSMOW scale (Polissar and D'Andrea, 2013). Plotted analytical uncertainties are the appropriate statistic for comparison between samples while the total uncertainties are appropriate for comparison to other studies.

3.6. Sediment age

Surface sediments from Paru Co were dated using ^{210}Pb , ^{214}Pb and ^{137}Cs measured by direct gamma counting on 24 samples from the upper 25 cm the surface core (Table 1; Appleby and Oldfield, 1983; Schelske et al., 1994). Radiocarbon age determination by accelerator mass spectrometry (AMS ^{14}C) was conducted on seven samples of carbonized grass fragments and one sample of oogonia after isolation from sediment intervals by wet sieving at $63\ \mu\text{m}$ (Table 2). All samples were manually cleaned and chemically pretreated according to standard protocols (Abbott and Stafford, 1996). We report the median probability age and 2σ error after calibration to thousands of calendar years before present (ka; present = AD 1950) with the online program CALIB 6.0 (Stuiver and Reimer, 1993) using the IntCal 09.14c data set.

4. Results

The Paru Co data presented here are archived at the National Climatic Data Center: http://hurricane.ncdc.noaa.gov/pls/paleox/f?p=519:1:::P1_STUDY_ID:16399

4.1. Core description and chronology

Light to dark tan bands ranging between 1 and 4 cm in thickness are present from 435 to 372.5 cm with two prominent black bands between 384.5 and 378.5 cm. From 372.5 to 140 cm, the bands increase in thickness, ranging between 3 and 10 cm, and are generally a darker tan to brown with intervals that are mottled and light tan. From 140 cm to the top of the core, the sediments are more homogeneous in appearance, alternating between lighter and darker shades of brown at 10 to 20 cm intervals.

Table 1
Lead-210 and ¹³⁷Cs results for Paru Co surface core A-11.

Depth interval (cm)	Pb-210 activity (Bq/g)	±1σ	Pb-214 activity (Bq/g)	±1σ	Cs-137 activity (Bq/g)	±1σ	Excess Pb-210 activity (Bq/g)	±1σ
0.25	0.687	0.170	0.268	0.06	<DET	<DET	0.419	0.110
0.75	0.604	0.135	0.375	0.05	<DET	<DET	0.229	0.088
1.25	0.593	0.122	0.231	0.03	<DET	<DET	0.362	0.088
1.75	0.551	0.133	0.447	0.05	<DET	<DET	0.104	0.081
2.25	0.648	0.1305	0.35	0.04	<DET	<DET	0.298	0.087
2.75	0.474	0.116	0.315	0.04	<DET	<DET	0.159	0.077
3.25	0.556	0.187	0.326	0.05	<DET	<DET	0.230	0.133
3.75	0.589	0.122	0.306	0.04	<DET	<DET	0.283	0.082
4.25	0.479	0.1285	0.228	0.04	<DET	<DET	0.251	0.090
4.75	0.339	0.1365	0.323	0.05	<DET	<DET	0.016	0.088
5.25	0.535	0.0905	0.196	0.02	<DET	<DET	0.339	0.066
6.25	0.716	0.1365	0.161	0.04	<DET	<DET	0.555	0.093
6.75	0.299	0.1025	0.206	0.03	<DET	<DET	0.093	0.069
7.25	0.469	0.0965	0.263	0.03	0.0526	0.01665	0.206	0.064
7.75	0.442	0.095	0.161	0.03	<DET	<DET	0.281	0.063
8.75	0.498	0.1025	0.171	0.03	<DET	<DET	0.327	0.070
9.25	0.401	0.100	0.080	0.018	<DET	<DET	0.321	0.083
10.75	0.347	0.072	0.175	0.024	0.064	0.015	0.172	0.048
13	0.434	0.095	0.141	0.029	0.061	0.020	0.293	0.066
15	0.349	0.085	0.143	0.028	0.055	0.018	0.206	0.056
17.75	<DET	<DET	0.078	0.016	<DET	<DET	<DET	<DET
20	<DET	<DET	0.079	0.024	<DET	<DET	<DET	<DET
22	<DET	<DET	0.140	0.025	<DET	<DET	<DET	<DET
25	<DET	<DET	0.113	0.031	<DET	<DET	<DET	<DET

Table 2
Radiocarbon ages from Paru Co.

UCIAMS #	Core	Drive	Mean depth (cm)	Material	Fraction modern	±	Δ ¹⁴ C (‰)	±	¹⁴ C age (BP)	±	Median cal age (ka)	±
104264	A-11		33.5	Oogonia	0.8647	0.0016	−135.2998	1.6120	1170	15	1093	15
99767	B-11	1	90.5	Charcoal	0.7607	0.0046	−239.3492	4.6442	2200	50	2220	50
99768	B-11	1	140.5	Charcoal	0.6353	0.0036	−364.7356	3.6460	3645	50	3970	50
99769	B-11	3	214.6	Charcoal	0.5070	0.0009	−492.9795	0.9387	5455	15	6270	15
104265	B-11	3	295.1	Charcoal	0.3675	0.0031	−632.5395	3.1243	8040	70	8900	70
104266	B-11	6	364.1	Charcoal	0.3075	0.0014	−692.4757	1.3838	9475	40	10721	40
*104267	B-11	6	388.6	Charcoal	0.1630	0.0048	−836.9894	4.7653	14570	240	17721	240
104268	B-11	6	434.9	Charcoal	0.3030	0.0032	−696.9967	3.1960	9590	90	10936	90

* Excluded from age model

Between 0.0 and 15.0 cm, excess ²¹⁰Pb averages $0.26 \pm 1 \text{ Bq g}^{-1}$ with a variable decay trend (Fig. 3a; Table 1). Peak ¹³⁷Cs occurs between 7.25 and 15.0 cm, with a maximum at 10.75 cm, suggesting this interval dates to AD 1963 in accordance with the cessation of atmospheric nuclear weapons testing. Although peak ¹³⁷Cs agrees with the ²¹⁰Pb age model, the ²¹⁰Pb decay profile suggests some mixing of the uppermost sediments.

Seven of the AMS ¹⁴C ages are in stratigraphic order, including the oogonia sample, indicating a basal age of 10.9 ka (Fig. 3b). The charcoal sample at 411.4 cm returned an age of 17.7 ka. This anomalous age was excluded from the age model because it is bracketed by dates in chronostratigraphic order. The final age model was constructed using linear regression between 434.9 and 364.1 cm and by fitting a 3rd order polynomial to the AMS ¹⁴C, ¹³⁷Cs (−0.013 ka) and sediment–water interface (−0.061 ka) ages between 364.1 and 0.0 cm (Fig. 3b).

4.2. Sedimentology

Sedimentation rates were highest at Paru Co from 10.9 to 10.7 ka, averaging 3.23 mm yr^{-1} (Fig. 4a). After 10.7 ka, sedimentation rates decreased by almost an order of magnitude to 0.34 cm yr^{-1} . Bulk densities vary between 0.501 and 0.037 g cm^{-3} with the highest values between 10.9 and 10.7 ka (Fig. 4a). After 10.7 ka, ρ_{dry} decreased gradually and was variable until 0.7 ka.

From 0.7 ka to the present, ρ_{dry} decreased sharply. Total organic matter varies between 12.2 and 56.6% with the lowest values from 10.9 to 10.7 ka (Fig. 4b). Between 10.7 and 0.7 ka, %TOM increased steadily with some variability, rising sharply after 0.7 ka. Total carbonate was below detection limits. The lithic fraction varies between 87.5 and 22.8% with the lithic flux closely tracking %Lithics ($r^2 = 0.84$; Fig. 4c). Maximum lithic flux occurred from 10.9 to 7.1 ka with values ranging between 0.161 and $0.008 \text{ g cm}^{-2} \text{ yr}^{-1}$. With the exception of a peak between 5.7 and 5.2 ka, the lithic flux decreased after 7.1 ka to minimum values at 3.4 ka. After 3.4 ka, lithic flux increased with a particularly sharp rise between 1.8 and 0.7 ka and subsequent reduction to the present. Analytically determined and estimated %BSi show a good correspondence during the Holocene ($r^2 = 0.68$; Fig. 4d), varying between 51.2 and 0.5%. Minimum, but variable, %BSi between 10.9 and 7.1 ka was followed by a maximum in %BSi between 7.1 and 3.4 ka that was briefly interrupted by a decrease from 5.7 to 5.2 ka. After 3.4 ka, %BSi decreased, reaching modern values by 1.8 ka.

4.3. Grain size

Grain size results were categorized into 46 bins between 0.1–0.49 μm and 1000–2000 μm and are presented as percent abundance (Fig. 4e). Principal component analysis (PCA) of the grain size correlation matrix was conducted in order to extract

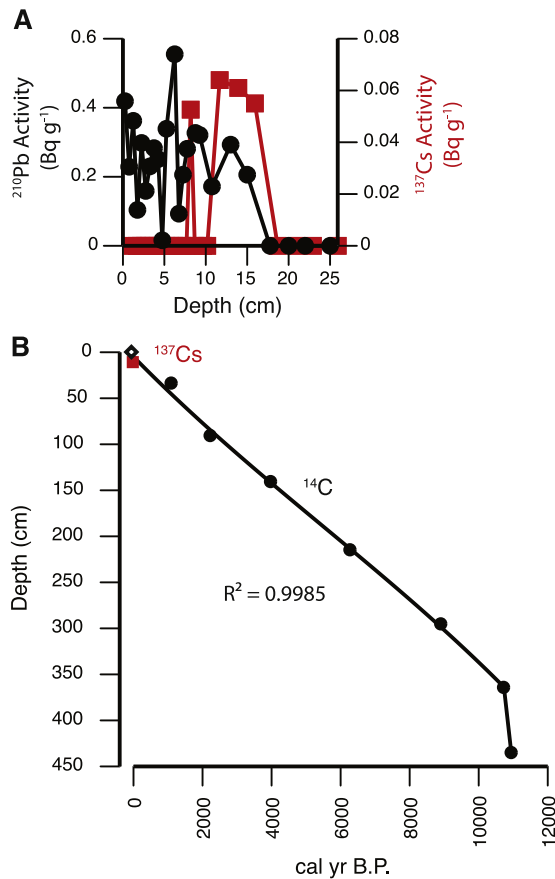


Fig. 3. (a) Results for ^{210}Pb (black) and ^{137}Cs (red) measurements from Paru Co. (b) The final Paru Co age model with AMS ^{14}C ages depicted by black circles (errors are smaller than the symbols). The red square marks the depth of the 1963 ^{137}Cs peak, and the open diamond marks the modern sediment water interface (2011 AD). (For interpretation of the references to color in this figure legend, the reader is referred to the web version of this article.)

covariability between the grain size fractions that may not be adequately captured by the traditional clay, silt and sand groupings. Variables with loadings ≤ 0.5 were suppressed in the output of the unrotated PCA (Fig. 5).

The first PC (PC1) explains 41.66% of the grain size variance and is characterized by positive loadings of fine clay to fine silt (0.58–11.00 μm) and negative loadings of coarse silt and fine sand (22.10–125.00 μm ; Fig. 4f). PC1 shows considerable variability between 10.9 and 5.2 ka with positive excursions from 10.1–9.1, 8.6–7.8, 7.6–6.7, 6.4–5.9 and 5.7–5.2 ka and corresponding negative excursions between. After 5.2 ka, PC1 shows less variability with values near 0 until 2 ka, at which point it decreases to a late Holocene minimum at 1.4 ka before increasing to modern values by 0.3 ka.

The second PC (PC2) accounts for 22.99% of the grain size variance and is characterized by positive loadings of fine clay (0.49–1.95 μm) and very fine to fine sand (63.00–149.00 μm ; Fig. 4g). Very fine to medium silt (7.80 and 22.10 μm) is negatively loaded on PC2. PC2 is generally negative between 10.7 ka and 5.7 ka, but with an increasing tendency toward positive values after 6.8 ka. After 5.7 ka, PC2 is positive with reduced variability until 1.3 ka, at which point it abruptly turns negative before sharply increasing again after 0.2 ka.

4.4. δD_{wax}

δD_{wax} results of the C-27 and C-29 *n*-alkanes are presented as raw and corrected values and discussed as the average of the cor-

rected isotopic profiles (Fig. 4h). The modern isotopic fractionation (ϵ_a) between precipitation (δD_{precip}) and δD_{wax} due to plant vital effects for the Tibetan Plateau may be smaller (50 to 90‰; Xia et al., 2008) than that reported for other alpine regions (Polissar and Freeman, 2010). Modeled annual average δD_{precip} has a value of -118‰ (Bowen et al., 2005), which is consistent with the δD of modern Paru Co lake water (-118‰). The uppermost sample from Paru Co (3.5 cm) has a δD_{wax} value of -203‰ , suggesting an ϵ_a of 85‰ between δD_{wax} and δD_{precip} . This falls within the previously measured range and so is applied to the Paru Co data (Xia et al., 2008). Vegetation changes are assumed to exert a negligible influence on ϵ_a because pollen work on nearby Hidden Lake shows that the dominant vegetation types were present throughout the Holocene and the timing of vegetation transitions do not correspond to changes in δD_{wax} (Tang et al., 2000).

δD_{wax} values vary between -158 and -115‰ with the high values between 10.9 and 10.7 ka. δD_{wax} rapidly decreased after 10.7 ka, reaching minimum values between 10.1 and 6.5 ka (Fig. 4h). After 6.5 ka, δD_{wax} increased through the Holocene with the exception of a slight lowering at 0.9 ka. High δD_{wax} values characterize the present (0.01 ka).

5. Discussion

5.1. Paru Co's depositional environment

Based on sedimentation rates and ρ_{dry} , we divided the Paru Co record into two periods, one from 10.9 to 10.7 ka and one from 10.7 ka to the present (Fig. 4a). Elevated sedimentation rates and ρ_{dry} from 10.9 to 10.7 ka likely reflect glacial sedimentation at Paru Co during the early Holocene. Significant reductions in ρ_{dry} and the stabilization of sedimentation rates after 10.7 ka suggests that glacial activity ended in the Paru Co watershed at this time and that the catchment remained unglacierized during the Holocene. Variability in Paru Co's sediment constituents from 10.7 to the present is therefore considered to reflect climatic, not glacial processes. Because the climate of the Nyainqentanglha Mountains is dominated by the ISM and deposition only occurs at Paru Co during the boreal summer when the lake is ice-free, we interpret sedimentological variability after 10.7 ka to reflect summer climatic conditions and variations in ISM rainfall.

Sediments deposited in Paru Co are comprised of allochthonous and autochthonous organic matter, biogenic silica and lithic material. The lithic and %BSi fractions show considerable variability that is anti-phased throughout the Holocene ($r^2 = 0.85$). This relationship likely reflects both a dilution and productivity effect that is proportional to the abundance of clastic material entering the lake and its influence on water column turbidity and diatom productivity. The anti-phased relationship between lithics and %BSi explains the near constant sediment accumulation rates during the Holocene, whereby an increase (decrease) in lithic flux was offset by a decrease (increase) in %BSi. In contrast, %TOM shows relatively little variability superimposed on its increasing Holocene trend. This indicates that Paru Co's depositional environment is dominated by variations in the delivery of clastic material.

We suggest that the delivery of lithics to Paru Co is driven by ISM rainfall such that more intense rainfall results in greater lithic deposition, and vice versa. Spring snow melt likely contributes to sediment transport and deposition at Paru Co, but given the dominance of summer (90%) over winter (10%) precipitation, we argue that the primary signal captured by variations in lithic flux is related to ISM rainfall intensity.

Following this first order interpretation, the lithic data suggests that ISM rainfall was enhanced during the early Holocene between 10.1 and 7.1 ka and that it decreased to a minimum between 7.1

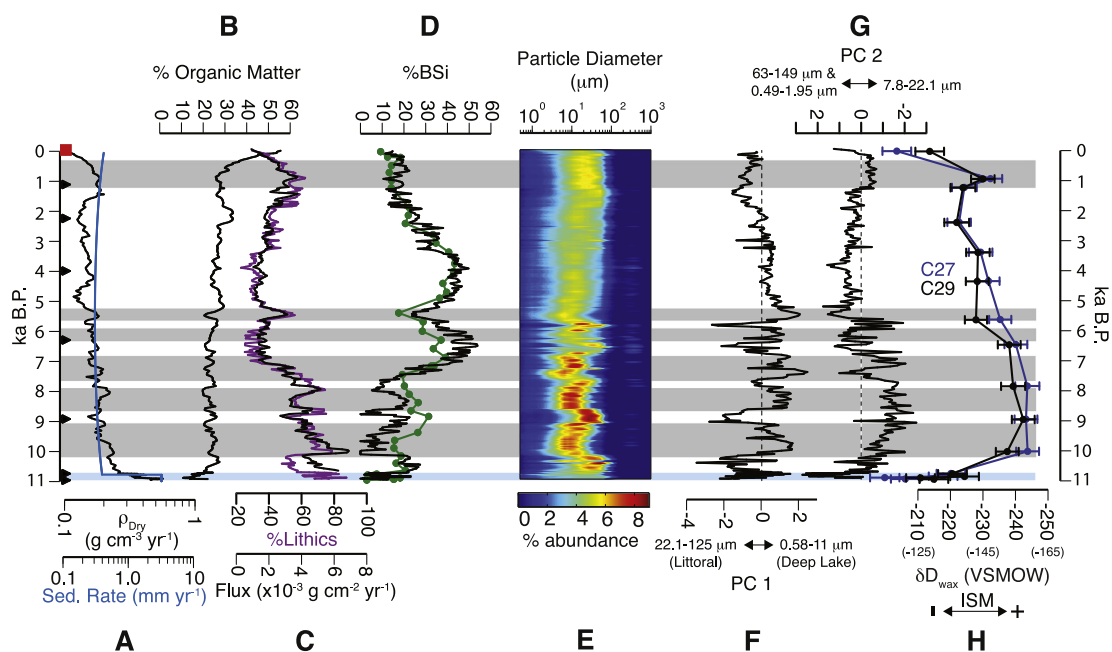


Fig. 4. Results from Paru Co showing (a) sedimentation rates (blue) and dry bulk density (black), (b) %total organic matter, (c) %lithics (purple) and lithic flux (black), (d) estimated (black) and analytically determined (green) %BSi, (e) particle size abundance distributions, (f) PC1, (g) PC2, (h) δD_{wax} results for the C-27 and C-29 *n*-alkanes showing raw and corrected (in parentheses) values. The blue rectangle marks the interval during which glacial sedimentation dominated the Paru Co depositional environment. Grey boxes indicate periods of high lake stands and/or strengthened ISM rainfall. The black triangles and red square mark the location of AMS ^{14}C and ^{137}Cs dates on the time axis, respectively. (For interpretation of the references to color in this figure legend, the reader is referred to the web version of this article.)

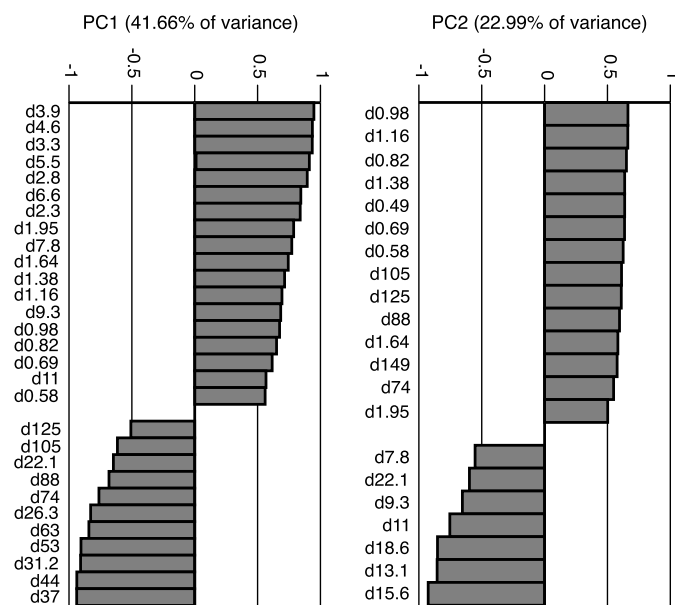


Fig. 5. Factor correlations for PC1 and PC2 from the unrotated PCA of the Paru Co grain size matrix. Factors scoring less than 0.5 were suppressed in the output. “d” represents the grain size diameter in microns.

and 3.4 ka, although with a possible century-scale increase between 5.7 and 5.2 ka (Fig. 4c). ISM rainfall then increased during the late Holocene in two steps at 3.4 and 1.9 ka, followed by a decrease again after 0.3 ka.

5.2. δD_{wax} interpretation and trends

Below freezing temperatures in the Nyainqentanglha Mountains from November through April restricts productivity in the Paru Co watershed to the summer months when the ISM is also at its peak. As a result, leaf waxes are produced and transported to Paru Co during this time. Recent studies of surface waters (Tian et al., 2003,

2007) and isotope-enabled climate models (Vuille et al., 2005; LeGrande and Schmidt, 2009; Pausata et al., 2011) show that ISM variability exerts a strong control on the isotopic composition of summer precipitation over India and the southern Tibetan Plateau through convection, distillation, the degree of rainout and orographic effects during moisture transport. δD_{wax} variability in the Paru Co record thus reflects large-scale processes associated with regional ISM dynamics, and not simply the local rainfall amount. Consequently, δD_{wax} is lower when the ISM is enhanced and higher when it is weaker.

The transition from high to low δD_{wax} by 10.1 ka signifies a rapid strengthening of the ISM during the early Holocene as glaciers retreated (Fig. 4h). Minimum δD_{wax} from 10.1 to ~6.5 ka indicates that ISM rainfall remained enhanced during the early and middle Holocene. δD_{wax} increased by 5.6 ka, suggesting that the ISM weakened by this time. This drying trend is interrupted briefly by a modest decrease in δD_{wax} at 0.9 ka, which suggests that the ISM strengthened slightly at this time within the context of a weakened mean state.

The δD_{wax} record generally tracks the lithics data, supporting the idea that the delivery of clastic material to Paru Co was indeed linked to changes in the strength of the ISM over the Paru Co watershed. Even the late Holocene increase in lithic flux corresponds well with the decrease in δD_{wax} at 0.9 ka. The early decrease in lithic flux to Paru Co (7.1 ka) relative to the increase in δD_{wax} by 5.6 ka, however, suggests that the intensity ISM rainfall diminished locally before it weakened synoptically.

5.3. Grain size interpretation and trends

The primary mode of grain size variability as captured by PC1 reflects the interplay between the deposition of fine and coarse sediments (Fig. 4e and f). Importantly, the PC1 grain size variability does not resemble either the lithic flux or the δD_{wax} trends, indicating that processes other than delivery of clastic material to the lake by runoff controlled grain size variations. We suggest that PC1 reflects oscillations between two end member depositional envi-

ronments with fines indicative of deep lake conditions and coarser material reflective of shallower lake conditions (i.e., littoral zone sediments). During high lake stands, the core site would have been more distal to the littoral zone and the point where runoff enters the lake basin. As a result, coarse-grained sediment would be confined to the near shore portion of the lake basin and only fine sediment would be transported to the core location. Conversely, during shallow lake conditions, the core site would become more proximal to both the littoral zone and the point where runoff enters the lake, thereby increasing the energy of the depositional environment (i.e., through the influence of the littoral wave base) and the grain size of sediments deposited (e.g., Håkanson, 1982). Following this line of reasoning, we interpret greater abundances of clay to reflect high lake stands as result of generally wetter conditions and increases in coarse material as indicative of lower lake stands during periods of drier conditions when effective moisture was reduced and the lake contracted (e.g., Shuman et al., 2009).

Following this interpretation, we identify five century-scale high lake stands between 10.1 and 5.2 ka with intervening low stands (Fig. 4f). After 5.2 ka, lake levels decreased, but remained stable until 1.9 ka, when they decreased to their Holocene minimum at 1.4 ka. Lake levels then increased to their present level by 0.3 ka.

Our interpretation of PC1 as an indicator of relative lake levels is consistent with the grain size trends captured by PC2 (Fig. 4). Low sand abundances and enhanced silt deposition between 10.1 and 5.7 ka associated with PC2 is consistent with generally higher lake levels during the early Holocene and enhanced sediment delivery to Paru Co indicated by PC1, peak lithic flux to Paru Co and minimum δD_{wax} values, respectively. Low abundances of fine clay during pluvial phases as indicated by PC2 may reflect greater export of fine sediments from the Paru Co depositional system as a result of seasonal or permanent overflowing conditions. Alternatively, the fine clay trends may reflect reduced dust deposition during pluvial phases and vice versa, even though fine clay is not the primary dust grain size (e.g., Conroy et al., 2013). Consistent with the grain-size lake-level model, very fine to fine sand abundances increased during the middle Holocene as δD_{wax} increased and PC1 and lithic flux decreased, suggesting diminished ISM rainfall reduced clastic (i.e., silt) deposition and lowered lake levels, which led to an encroachment of the littoral zone on the core site and an increase in sand deposition. Increasing lake levels after 1.4 ka corresponds to a decrease in very fine to fine sand deposition, which again is consistent with the hypothesized grain size response to lake-level change.

The consistency of the above trends supports our multi-proxy ISM reconstruction and the assertion that PC1 represents lake-level changes at Paru Co. It is important to stress, however, that these lake-level trends are qualitative. Even though low lake stands during the early Holocene have loadings on PC1 that are more negative than the most recent portion of the Paru Co record (when the lake is ~1 m deep), this does not necessarily imply that Paru Co was dry during the early Holocene. Indeed, there is no sedimentological evidence for desiccation at Paru Co and sediment deflation is not supported by the nearly linear age model. One possibility is that the core site was more sensitive to lake-level variations during the early Holocene because it was more distal to the littoral zone. Changes in the littoral zone wave base may therefore have produced a more discernable sedimentological signal when lake levels decreased. Conversely, during the late Holocene when the core site was on average more proximal to the littoral zone, variations in the littoral zone wave base would have produced less pronounced sedimentological variations. This threshold sensitivity to lake levels may in part explain reduced apparent lake-level variability after 5.2 ka. It is also possible that less intense ISM rainfall during the late Holocene narrowed the range of grain sizes trans-

ported to Paru Co, resulting in less extreme grain size variability and hence less apparent lake-level variability in PC1.

5.4. Comparison with Third Pole records

The Paru Co results agree well with existing records of ISM and climatic variability from the Tibetan Plateau (Fig. 6). Similarities between the Paru Co δD_{wax} record and lacustrine calcite oxygen isotope ($\delta^{18}O$) records from Lakes Qinghai (Lister et al., 1991), Seling Co (Gu et al., 1993) and Bangong Co (Gasse et al., 1996) are especially striking because age control for these records is sparse and bulk sediment dates were corrected for large reservoir effects. Regardless, these records all transition from high to low isotopic values during the early Holocene in accord with the Paru Co δD_{wax} record. The timing of this transition is later at Seling Co and Bangong Co by ~600 and ~800 yr, respectively, but this is within age model uncertainties and suggests synchronous strengthening of the ISM across the Tibetan Plateau. Consistent with the Paru Co δD_{wax} record, Lake Qinghai, Seling Co and Bangong Co show a broad early to middle Holocene minimum in isotopic values, suggesting a sustained period of enhanced ISM rainfall on the Tibetan Plateau. Increases in isotopic values at all sites after between 5 and 4 ka further signify a coherent weakening of ISM rainfall. Only the Bangong Co record shows an abrupt increase in $\delta^{18}O$ during the late Holocene. This may indicate a reduction in the westward extent of the ISM that resulted in western isotopic records becoming influenced by controls other than the ISM. Notably, each of these records shows a slight decreasing trend during the late Holocene when the Paru Co δD_{wax} decreased and the lithic flux increased, suggesting a coherent period of slightly enhanced ISM precipitation on a regional scale.

The above isotopic trends are broadly consistent with a recent high-resolution speleothem $\delta^{18}O$ record from Tianmen Cave that spans the period from 9.1 to 4.3 ka and 0.97 to 0.75 ka, supporting regionally coherent ISM trends (Fig. 6i). Notably, the resumption of calcite deposition at Tianmen Cave between 0.97 and 0.75 ka after a late Holocene hiatus corresponds with decreased δD_{wax} at Paru Co and an increased lithic flux and silt deposition. This supports a modest strengthening of the ISM during the late Holocene, despite generally dry regional conditions. The Hongyuan Bog, Lake Naleng and Ximencuo records also support the idea of broadly contemporaneous ISM patterns at millennial timescales with warmer and wetter conditions during the early Holocene between ~11 and 5 ka transitioning to cooler and drier conditions after this time (Hong et al., 2003; Kramer et al., 2010; Mischke and Zhang, 2010).

The Paru Co results are also similar to several regional lake-level reconstructions, including Ahung Co (Morrill et al., 2006), Zhari Namco (Chen et al., 2013), Donggi Conna (Dietze et al., 2013) and others from across the Tibetan Plateau (Fig. 6; Hudson and Quade, 2013). In general, high lake levels occurred across the Tibetan Plateau during the early Holocene with a subsequent trend toward significantly lower lake levels and volumes to the present. The Ahung Co reconstruction, which is based on PCA analysis of multi-proxy sediment data and is the closest to Paru Co, suggests maximum lake levels between 9 and 7.5 ka with decreasing lake levels after this time until ~4 ka when deposition in the lake basin ceased (Fig. 6g). These trends closely track the Paru Co lithic data, which indicate maximum clastic deposition during the early Holocene until 7.1 ka. The Paru Co PC1 lake-level curve shows greater lake-level variability during the early and middle Holocene, however, with high stands occurring until 5.2 ka. The δD_{wax} data further suggest that ISM rainfall remained enhanced until ~5.5 ka. Differences between the Paru Co and Ahung Co records may reflect local precipitation/evaporation (P/E) balance differences, changes in the spatial extent of the ISM through time, or that the Ahung

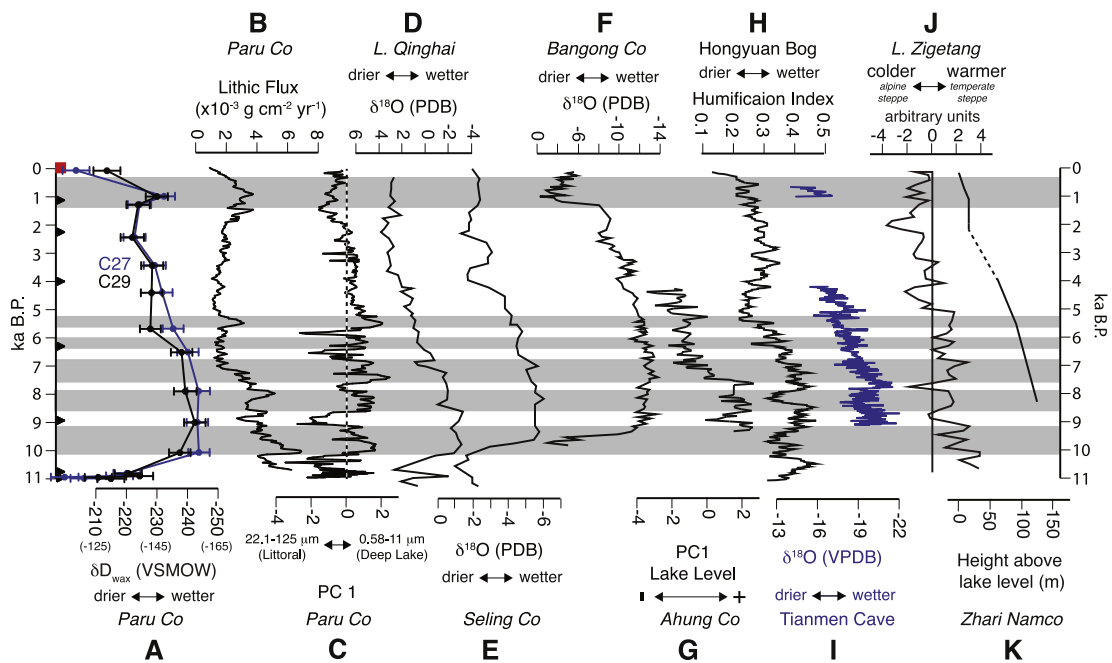


Fig. 6. The Paru Co (a) δD_{wax} results, (b) lithic flux and (c) PC1 lake-level reconstruction are compared with (d) Lake Qinghai $\delta^{18}O$, (e) Seling Co $\delta^{18}O$, (f) Bangong Co $\delta^{18}O$, (g) the Ahung Co PC1 lake-level reconstruction, (h) the Hongyuan Bog humification index, (i) Tianmen Cave $\delta^{18}O$, (j) the Lake Zigetang relative temperature curve and (k) Zhari Namco lake levels relative to the present. Gray boxes indicate periods of high lake stands and/or intensified ISM rainfall based on the Paru Co data. Age control is displayed on the y-axis as in Fig. 5. Cave records are colored blue, lake and bog records are black. (For interpretation of the references to color in this figure legend, the reader is referred to the web version of this article.)

Co PC1 captures changes in other factors that are related to ISM rainfall, like runoff and sediment delivery, in addition to lake-level changes.

Lake-level variability at Paru Co inferred from PC1 corresponds well with a pollen based temperature reconstruction from Lake Zigetang (Fig. 6j; Herzschuh et al., 2006). Each high lake stand between 10.1 and 5.2 ka corresponds to an interval of inferred warmth while intervening low stands coincide with cool episodes. The broader Holocene lake-level pattern is also consistent with this temperature-lake level relationship where cooler temperatures at Lake Zigetang after ~ 5 ka coincided with lower lake levels and reduced lake-level variability at Paru Co (Fig. 6c and j). Additionally, minimum Paru Co lake levels at 1.4 ka and the subsequent increase broadly track the shift from minimum late Holocene temperatures at Lake Zigetang to warmth more characteristic of the modern environment. The relationship between these records suggests that lake levels were closely connected to temperatures on the Tibetan Plateau, even if isotopic evidence suggests that synoptic-scale ISM variability was not greatly affected by these cool episodes. Notably, high-frequency variability in the Tianmen Cave $\delta^{18}O$ record occurs in phase with the Lake Zigetang temperature excursions, where cool episodes correspond to lower $\delta^{18}O$ values and warm excursions correspond to high $\delta^{18}O$ values (Fig. 6i and j). This might suggest that temperature and/or winter precipitation affected high-frequency Tianmen Cave $\delta^{18}O$ variability, but that the millennial trends capture general changes in ISM rainfall.

Beyond the Third Pole Environment, the Paru Co results are compared with Mawmluh Cave, India (Fig. 7d; Berkelhammer et al., 2012), a low elevation record that captures the isotopic composition of ISM rainfall prior to orographic uplift and delivery to the Tibetan Plateau. Immediately apparent is that $\delta^{18}O$ at Mawmluh Cave remained high between 11 and 8.5 ka, suggesting ISM rainfall was reduced over the Indian subcontinent, while isotopic and sedimentological data from Tibet suggest the ISM was enhanced during this time. At 8.5 ka, $\delta^{18}O$ decreased at Mawmluh Cave and remained low, although with considerable variability, until ~ 5.6 ka, reflecting enhanced low elevation ISM rainfall. Although δD_{wax} at

Paru Co increased at about the same time as $\delta^{18}O$ at Mawmluh Cave, lake levels remained high at Paru Co until 5.2 ka. Regardless, both records support a shift to reduced ISM rainfall during the middle Holocene by between 5.6 and 5.2 ka. A prominent shift in the Mawmluh Cave record to high $\delta^{18}O$ at ~ 4 ka was followed by a cessation of calcite deposition that coincides with increasing δD_{wax} at Paru Co and hiatuses in the Ahung Co and Tianmen Cave records. This suggests a coherent regional weakening in the ISM during the transition to the late Holocene, which is consistent with previous findings (Morrill et al., 2003).

5.5. Millennial Holocene ISM forcing

Coherent ISM variability over the Tibetan Plateau during the Holocene suggests a common, synoptic-scale forcing mechanism. Accordingly, the Paru Co results are in good agreement with Intertropical Convergence Zone (ITCZ) reconstructions from the Indian (Fleitmann et al., 2007) and Atlantic Oceans (Haug et al., 2001), where the ISM maximum between 10.1 and ~ 5.5 ka occurred when the ITCZ was at its most northward Holocene position and the transition to a weakened ISM during the middle and late Holocene tracks the southward migration of the ITCZ (Fig. 7f and g). This supports an important role for the ITCZ in ISM variability through the delivery of Indian Ocean moisture and its influence on deep convection over land (Gadgil, 2003).

Millennial-scale ISM and ITCZ trends also track changes in the zonal structure of tropical Pacific sea surface temperatures (SSTs) that resemble the spatial patterns of ENSO (El Niño-Southern Oscillation; Fig. 7h and i). Consistent with the modern ISM response to ENSO (Ashok et al., 2004b), peak ISM rainfall during the early Holocene occurred in conjunction with a northerly ITCZ and La Niña-like zonal SSTs gradients with cooler conditions in the eastern tropical Pacific cold tongue (Koutavas et al., 2006; Marchitto et al., 2010) and warmer conditions in the Indo-Pacific warm pool (Stott et al., 2004; Linsley et al., 2010). Conversely, the ISM weakened during the middle Holocene as zonal SST gradients decreased at ~ 5 ka and the ITCZ migrated southward.

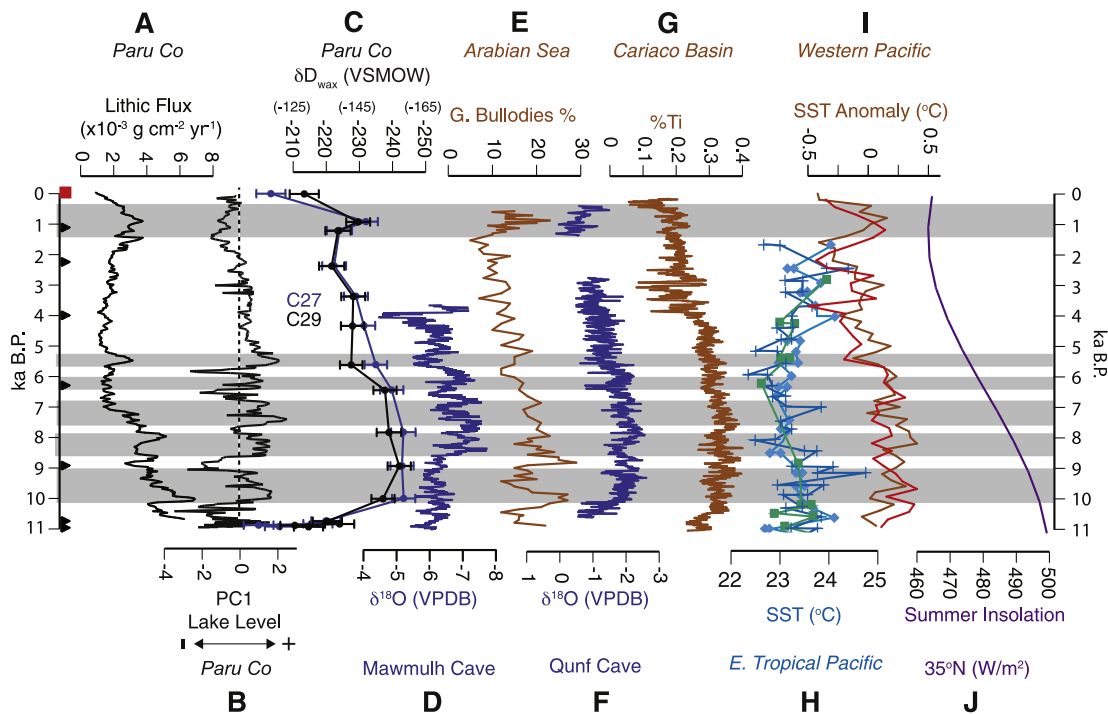


Fig. 7. Comparison of the Paru Co (a) lithic flux, (b) PC1 relative lake-level curve and (c) δD_{wax} results with (d) the Mawmulh Cave $\delta^{18}O$ ISM record, (e) the Dongge Cave $\delta^{18}O$ Asian monsoon record, (f) the Qunf Cave $\delta^{18}O$ record of the Indian Ocean ITCZ, (g) %Ti from the Cariaco Basin, a proxy for the Atlantic ITCZ (h) upwelling in the Arabian Sea based on *G. bullioides* abundance, (i) average eastern (blue and green) and western (red and orange) tropical Pacific SSTs and (j) summer insolation at 35°N (purple line). As in Fig. 6, the gray boxes indicate periods of high lake stands and/or strengthened ISM rainfall based on the Paru Co record. Lake records are colored black, cave records blue and marine records are in light brown, with the exception of the Pacific SST time series. (For interpretation of the references to color in this figure legend, the reader is referred to the web version of this article.)

The observed ISM-ITCZ-SST relationships support the idea that the position of the ITCZ contributes to ENSO-like SST gradients through evaporative feedbacks in the eastern tropical Pacific (Koutavas et al., 2006; Takahashi and Battisti, 2007) and that these interactions impacted the ISM. A northerly position of the ITCZ, such as during the early Holocene, would favor cooling in the eastern tropical Pacific cold tongue through evaporation and wind-driven upwelling, thereby suppressing warm ENSO events while a southerly ITCZ would promote reduced evaporation and upwelling, resulting in more El Niño-like conditions (i.e., the middle and late Holocene). This idea consistent with the modeled response of the Pacific to insolation forcing (Clement et al., 1996, 1999) as well as with ENSO proxy records that suggest La Niña-like conditions were prevalent during the early Holocene and that modern El Niño variability did not arise until the middle Holocene between 7 and 5 ka (Rodbell et al., 1999; Moy et al., 2002; Rein et al., 2005).

5.6. Century scale Holocene ISM forcing

The Paru Co lake-level record (PC1) shows considerable centennial variability, particularly during the early Holocene. Although ENSO is an attractive explanatory mechanism, modeling and paleoclimate evidence suggest ENSO variability was attenuated during the early and middle Holocene (e.g., Moy et al., 2002). Other work has attributed centennial ISM variability to North Atlantic cooling (i.e., Bond Events) and/or solar variability, but the relationship with ice rafted debris and total solar irradiance reconstructions is not clear (Bond et al., 2001; e.g., Hong et al., 2003; Porter and Weijian, 2006; Cai et al., 2012).

An alternative synoptic scale mechanism capable of influencing the ISM is the Indian Ocean Dipole (Saji et al., 1999; Ashok et al., 2004a). Abram et al. (2009) presented a record of discrete SST anomalies (SSTAs) from corals located near Mentawai Island

off the coast of Sumatra, Indonesia, that support the occurrence of strong cooling between 5.5 and 4.3 ka, suggestive of positive IOD event. This event coincided with increased lithic flux during the 5.6–5.2 ka Paru Co lake high stand and warming on the central Tibetan Plateau. These conditions are consistent with positive IOD events, which increase moisture delivery to the Tibetan Plateau and strengthen the ISM as a result of enhanced easterlies and cross equatorial return flow over the northern tropical Indian Ocean (Ashok et al., 2004b). Conversely, low lake levels at Paru Co during the early Holocene broadly correspond with warming events off the Java coast (Abram et al., 2009). This may reflect the occurrence of negative IOD events, which produce the opposite set of synoptic conditions and deficits in ISM rainfall, even during strong La Niña events (Ashok et al., 2004b). More continuous IOD records are needed, however, to better evaluate IOD–ISM interactions through the Holocene.

Meridional variations in the position of the ITCZ are another potential mechanism of centennial ISM variability. However, $\delta^{18}O$ from Qunf Cave and %Ti in the Cariaco Basin only support centennial-scale ITCZ forcing during the early and late Holocene. High $\delta^{18}O$ and low %Ti in these records from 10.9 to 10.1 ka coincide with maximum aridity in the Paru Co record suggesting a southerly ITCZ contributed to the weakened ISM state (Fig. 7). High %Ti between 1.1 and 0.6 ka and the resumption of calcite deposition between 1.3 and 0.3 ka after a ~1400-yr hiatus suggests a more northerly ITCZ at that time. This coincides with a decrease in δD_{wax} and increased lithic flux, silt deposition and lake levels at Paru Co, indicating that the ISM strengthened while the ITCZ was in a more northerly position. Upwelling records from the Arabian Sea further support strengthened monsoonal winds at this time, while SSTs in the Indo-Pacific were at their highest since 5 ka (Fig. 7e and i; Overpeck et al., 1996; Gupta et al., 2005).

Further work that combines modeling and paleoclimate investigations is needed to characterize the spatiotemporal patterns of hydroclimate variability on the Third Pole and characterize relationships with the tropical Indian Ocean, ITCZ and other components of the global climate system. We suggest that regional controls, like the IOD, are potentially important drivers of ISM variability, particularly during the early Holocene when ENSO was attenuated.

6. Conclusions

Sedimentological and δD_{wax} data from Paru Co provide an 11,000-yr perspective of local and synoptic-scale ISM variability on the southeastern Tibetan Plateau. Our results indicate that the ISM was considerably weaker between 10.9 and 10.7 ka, but rapidly strengthened to maximum intensity by 10.1 ka. Lithic flux data suggest rainfall intensity decreased at 7.1 ka, while δD_{wax} and grain size PC1 suggest ISM rainfall and effective moisture maxima continued until ~ 5.6 ka. Together, this supports a more prolonged ISM maximum on the Tibetan Plateau than some previous estimates (An et al., 2000; He et al., 2004). Following the early Holocene ISM maximum, local and synoptic ISM rainfall was reduced through the middle and late Holocene, increasing slightly after 3.4 ka and more so between ~ 1.9 and 0.3 ka. Consistency between the Paru Co data and other records from the Tibetan Plateau suggests coherent millennial ISM variability, but with an increasing magnitude from east to west. These low frequency changes in Holocene ISM rainfall largely track decreasing summer insolation, temperatures on the Tibetan Plateau, Indo-Pacific SSTs (including ENSO and the IOD) and the position of the ITCZ. Centennial ISM variability on the central Tibetan Plateau was closely linked to land surface temperatures, but may also reflect the increased importance of IOD variability, particularly during the early Holocene when ENSO was attenuated. The ITCZ may also have been important on century timescales during the early (10.9 to 10.1 ka) and late (1.9 to 0.3 ka) Holocene. Isotopic differences with the upstream Mawmulh Cave record suggests that ISM rainfall over the Tibetan Plateau and Indian subcontinent may respond differently to similar forcing mechanisms, a point that requires further investigation. Although additional proxy and modeling studies are needed to characterize the spatiotemporal expression of centennial and decadal ISM variability, we hypothesize that it is related to Indo-Pacific SSTs and Tibetan land surface temperatures.

Acknowledgements

Funding for this research was provided by the United States National Science Foundation (EAR-1023547) and the Chinese National Natural Science Foundation of China (Award 41150110153). Special thanks to Nima for his invaluable assistance with fieldwork and to Angela Robertson for her assistance with the perpetration and measurement of the grain size samples. We also thank John Southon at the University of California, Irvine, Keck Carbon Cycle AMS facility for his assistance with the radiocarbon dating and the Limnological Research Center at University of Minnesota. B.A.S acknowledges support from the US NSF AGS-PRF (AGS-1137750). We would also like to thank the three anonymous reviewers and Dr. Jean Lynch-Stieglitz for their comments on this work.

Appendix A. Supplementary data

Supplementary data associated with this article can be found in the online version at <http://dx.doi.org/10.1016/j.epsl.2014.05.017>. These data include the Google map of the most important areas described in this article.

References

- Abbott, M.B., Stafford, T.W., 1996. Radiocarbon geochemistry of modern and ancient Arctic lake systems, Baffin Island, Canada. *Quat. Res.* 45, 300–311.
- Abram, N.J., McGregor, H.V., Gagan, M.K., Hantoro, W.S., Suwargadi, B.W., 2009. Oscillations in the southern extent of the Indo-Pacific Warm Pool during the mid-Holocene. *Quat. Sci. Rev.* 28, 2794–2803.
- An, Z., Porter, S.C., Kutzbach, J.E., Xihao, W., Suming, W., Xiaodong, L., Xiaoqiang, L., Weijian, Z., 2000. Asynchronous Holocene optimum of the East Asian monsoon. *Quat. Sci. Rev.* 19, 743–762.
- Appleby, P.G., Oldfield, F., 1983. The assessment of ^{210}Pb data from sites with varying sedimentation accumulation rates. *Hydrobiologia* 103, 29–35.
- Ashok, K., Chan, W.L., Motoi, T., Yamagata, T., 2004a. Decadal variability of the Indian Ocean dipole. *Geophys. Res. Lett.* 31.
- Ashok, K., Guan, Z., Saji, N., Yamagata, T., 2004b. Individual and combined influences of ENSO and the Indian Ocean dipole on the Indian summer monsoon. *J. Climate* 17, 3141–3155.
- Berkehammer, M., Sinha, A., Stott, L., Cheng, H., Pausata, F.S.R., Yoshimura, K., 2012. An abrupt shift in the Indian monsoon 4000 years ago. In: *Climates, Landscapes, and Civilizations*. In: *Geophys. Monogr. Ser. AGU*, Washington, DC, pp. 75–87.
- Bond, G., Kromer, B., Beer, J., Muscheler, R., Evans, M.N., Showers, W., Hoffmann, S., Lotti-Bond, R., Hajdas, I., Bonani, G., 2001. Persistent solar influence on North Atlantic climate during the Holocene. *Science* 294, 2130–2136.
- Bowen, G.J., Wassenaar, L.I., Hobson, K.A., 2005. Global application of stable hydrogen and oxygen isotopes to wildlife forensics. *Oecologia* 143, 337–348.
- Cai, Y., Zhang, H., Cheng, H., An, Z., Edwards, R.L., Wang, X., Tan, L., Liang, F., Wang, J., Kelly, M., 2012. The Holocene Indian monsoon variability over the southern Tibetan Plateau and its teleconnections. *Earth Planet. Sci. Lett.* 335–336, 135–144.
- Chen, Y., Zong, Y., Li, B., Li, S., Aitchison, J.C., 2013. Shrinking lakes in Tibet linked to the weakening Asian monsoon in the past 8.2 ka. *Quat. Res.* 80, 189–198.
- Choubert, G., Faure-Muret, A., Chanteux, P., 1983. *Atlas géologique du monde*. In: Commission for the Geological Map of the World. Unesco.
- Clement, A.C., Seager, R., Cane, M.A., Zebiak, S.E., 1996. An ocean dynamical thermostat. *J. Climate* 9, 2190–2196.
- Clement, A., Seager, R., Cane, M., 1999. Orbital controls on the El Niño/Southern Oscillation and the tropical climate. *Paleoceanography* 14, 441–456.
- Conroy, J.L., Overpeck, J.T., Cole, J.E., Liu, K.-B., Wang, L., Ducea, M.N., 2013. Dust and temperature influences on glaciofluvial sediment deposition in southwestern Tibet during the last millennium. *Glob. Planet. Change*.
- Dietze, E., Wünnemann, B., Hartmann, K., Diekmann, B., Jin, H., Stauch, G., Yang, S., Lehmkuhl, F., 2013. Early to mid-Holocene lake high-stand sediments at Lake Donggi Cona, northeastern Tibetan Plateau. *China Quat. Res.* 79 (3), 325–336. <http://dx.doi.org/10.1016/j.yqres.2012.12.008>.
- Fleitmann, D., Burns, S.J., Mangini, A., Mudelsee, M., Kramers, J., Villa, I., Neff, U., Al-Subbary, A.A., Buettner, A., Hippler, D., Matter, A., 2007. Holocene ITCZ and Indian monsoon dynamics recorded in stalagmites from Oman and Yemen (Socotra). *Quat. Sci. Rev.* 26, 170–188.
- Gadgil, S., 2003. The Indian monsoon and its variability. *Annu. Rev. Earth Planet. Sci.* 31, 429–467.
- Gasse, F., Fontes, J.C., Van Campo, E., Wei, K., 1996. Holocene environmental changes in Bangong Co basin (Western Tibet). Part 4: discussion and conclusions. *Paleo-geogr. Palaeoclimatol. Palaeoecol.* 120, 79–92.
- Gray, A.B., Pasternack, G.B., Watson, E.B., 2010. Hydrogen peroxide treatment effects on the particle size distribution of alluvial and marsh sediments. *Holocene* 20, 293–301.
- Gu, Z., Liu, J., Yuan, B., Liu, T., Liu, R., Liu, Y., Zhang, G., 1993. The changes in monsoon influence in the Qinghai-Tibetan Plateau during the past 12,000 years. *Geochemical evidence from the L. Selin sediments*. *Chin. Sci. Bull.* 38, 61–64.
- Gupta, A.K., Das, M., Anderson, D.M., 2005. Solar influence on the Indian summer monsoon during the Holocene. *Geophys. Res. Lett.* 32, L17703.
- Håkanson, L., 1982. Bottom dynamics in lakes. *Hydrobiologia* 91, 9–22.
- Haug, G.H., Hughen, K., Sigman, D.M., Peterson, L.C., Rohl, U., 2001. Southward migration of the intertropical convergence zone through the Holocene. *Science* 293, 1304–1308.
- He, Y., Theakstone, W.H., Zhonglin, Z., Dian, Z., Tandong, Y., Tuo, C., Yongping, S., Hongxi, P., 2004. Asynchronous Holocene climatic change across China. *Quat. Res.* 61, 52–63.
- Heiri, O., Lotter, A.F., Lemcke, G., 2001. Loss on ignition as a method for estimating organic and carbonate content in sediments: reproducibility and comparability of results. *J. Paleolimnol.* 25, 101–110.
- Herzschuh, U., 2006. Palaeo-moisture evolution in monsoonal Central Asia during the last 50,000 years. *Quat. Sci. Rev.* 25, 163–178.
- Herzschuh, U., Winter, K., Wünnemann, B., Li, S., 2006. A general cooling trend on the central Tibetan Plateau throughout the Holocene recorded by the Lake Zige-tang pollen spectra. *Quat. Int.* 154–155, 113–121.
- Hong, Y.T., Hong, B., Lin, Q.H., Zhu, Y.X., Shibata, Y., Hirota, M., Uchida, M., Leng, X.T., Jiang, H.B., Xua, H., Wang, H., Yi, L., 2003. Correlation between Indian Ocean summer monsoon and North Atlantic climate during the Holocene. *Earth Planet. Sci. Lett.* 211, 371–380.

- Hudson, A.M., Quade, J., 2013. Long-term east-west asymmetry in monsoon rainfall on the Tibetan Plateau. *Geology* 41, 351–354.
- Huffman, G.J., Adler, R.F., Bolvin, D.T., Nelkin, E.J., 2010. The TRMM multi-satellite precipitation analysis (TMPA). In: *Satellite Rainfall Applications for Surface Hydrology*. Springer, pp. 3–22.
- Koutavas, A., Olive, G.C., Lynch-Stieglitz, J., 2006. Mid-Holocene El Niño–Southern Oscillation (ENSO) attenuation revealed by individual foraminifera in eastern tropical Pacific sediments. *Geology* 34, 993–996.
- Kramer, A., Herzschuh, U., Mischke, S., Zhang, C., 2010. Holocene treeline shifts and monsoon variability in the Hengduan Mountains (southeastern Tibetan Plateau), implications from palynological investigations. *Palaeogeogr. Palaeoclimatol. Palaeoecol.* 286, 23–41.
- LeGrande, A.N., Schmidt, G.A., 2009. Sources of Holocene variability of oxygen isotopes in paleoclimate archives. *Clim. Past* 5, 441–455.
- Linsley, B.K., Rosenthal, Y., Oppo, D.W., 2010. Holocene evolution of the Indonesian throughflow and the western Pacific warm pool. *Nat. Geosci.* 3, 578–583.
- Lister, G.S., Kelts, K., Zao, C.K., Yu, J.-Q., Niessen, F., 1991. Lake Qinghai, China: closed-basin like levels and the oxygen isotope record for ostracoda since the latest Pleistocene. *Palaeogeogr. Palaeoclimatol. Palaeoecol.* 84, 141–162.
- Marchitto, T.M., Muscheler, R., Ortiz, J.D., Carriquiry, J.D., van Geen, A., 2010. Dynamical response of the tropical Pacific Ocean to solar forcing during the early Holocene. *Science* 330, 1378–1381.
- Mischke, S., Zhang, C., 2010. Holocene cold events on the Tibetan Plateau. *Glob. Planet. Change* 72, 155–163.
- Morrill, C., Overpeck, J.T., Cole, J.E., 2003. A synthesis of abrupt changes in the Asian summer monsoon since the last deglaciation. *Holocene* 13, 465–476.
- Morrill, C., Overpeck, J.T., Cole, J.E., Liu, K.-b., Shen, C., Tang, L., 2006. Holocene variations in the Asian monsoon inferred from the geochemistry of lake sediments in central Tibet. *Quat. Res.* 65, 232–243.
- Mortlock, R.A., Froelich, P.N., 1989. A simple method for the rapid determination of biogenic opal in pelagic marine sediments. *Deep-Sea Res., A, Oceanogr. Res. Pap.* 36, 1415–1426.
- Moy, C.M., Seltzer, G.O., Rodbell, D.T., Anderson, D.M., 2002. Variability of El Niño/Southern Oscillation at millennial timescales during the Holocene epoch. *Nature* 420, 162–165.
- Overpeck, J., Anderson, D., Trumbore, S., Prell, W., 1996. The southwest Indian Monsoon over the last 18000 years. *Clim. Dyn.* 12, 213–225.
- Pausata, F.S.R., Battisti, D.S., Nisancioglu, K.H., Bitz, C.M., 2011. Chinese stalagmite $\delta^{18}\text{O}$ controlled by changes in the Indian monsoon during a simulated Heinrich event. *Nat. Geosci.* 4, 474–480.
- Peterson, T.C., Vose, R.S., 1997. An overview of the Global Historical Climatology Network temperature database. *Bull. Am. Meteorol. Soc.* 78, 2837–2849.
- Polissar, P.J., D'Andrea, W.J., 2013. Uncertainty in paleohydrologic reconstructions from molecular δD values. *Geochim. Cosmochim. Acta* 129, 146–156.
- Polissar, P.J., Freeman, K.H., 2010. Effects of aridity and vegetation on plant-wax δD in modern lake sediments. *Geochim. Cosmochim. Acta* 74, 5785–5797.
- Porter, S.C., Weijian, Z., 2006. Synchronism of Holocene East Asian monsoon variations and North Atlantic drift-ice tracers. *Quat. Res.* 65, 443–449.
- Rein, B., Luckge, A., Reinhardt, L., Sirocko, F., Wolfe, A., Dullo, W.-C., 2005. El Niño variability off Peru during the last 20,000 years. *Paleoceanography* 20, PA4003.
- Rodbell, D.T., Seltzer, G.O., Anderson, D.M., Abbott, M.B., Enfield, D.B., Newman, J.H., 1999. An ~15,000-year record of El Niño driven alluviation in southwestern Ecuador. *Science* 283, 516–520.
- Saji, N., Goswami, B.N., Vinayachandran, P., Yamagata, T., 1999. A dipole mode in the tropical Indian Ocean. *Nature* 401, 360–363.
- Schelske, C.L., Peplow, A., Brenner, M., Spencer, C.N., 1994. Low-background gamma counting: applications for ^{210}Pb dating of sediments. *J. Paleolimnol.* 10, 115–128.
- Shuman, B., Henderson, A.K., Colman, S.M., Stone, J.R., Fritz, S.C., Stevens, L.R., Power, M.J., Whitlock, C., 2009. Holocene lake-level trends in the Rocky Mountains, USA. *Quat. Sci. Rev.* 28, 1861–1879.
- Stott, L., Cannariato, K., Thunnell, R., Haug, G.H., Koutavas, A., Lund, S., 2004. Decline of surface temperature and salinity in the western tropical Pacific Ocean in the Holocene epoch. *Nature* 431, 56–59.
- Stuiver, M., Reimer, P.J., 1993. Extended ^{14}C database and revised CALIB radiocarbon calibration program. *Radiocarbon* 35, 215–230.
- Takahashi, K., Battisti, D.S., 2007. Processes controlling the mean tropical Pacific precipitation pattern. Part 1: the Andes and eastern Pacific ITCZ. *J. Climate* 20, 3434–3451.
- Tang, L., Shen, C., Liu, K., Overpeck, J.T., 2000. Changes in South Asian monsoon: New high-resolution paleoclimatic records from Tibet, China. *Chin. Sci. Bull.* 45, 87–91.
- The World Bank, 2012. *Disaster Risk Management in South Asia: A Regional Overview*.
- Tian, L., Yao, T., Schuster, P.F., White, J.W.C., Ichiyangi, K., Pendall, E., Pu, J., Yu, W., 2003. Oxygen-18 concentrations in recent precipitation and ice cores on the Tibetan Plateau. *J. Geophys. Res.* 108, 4293.
- Tian, L., Yao, T., MacClune, K., White, J.W.C., Schilla, A., Vaughn, B., Vachon, R., Ichiyangi, K., 2007. Stable isotopic variations in west China: a consideration of moisture sources. *J. Geophys. Res.* 112, D10112.
- Vuille, M., Werner, M., Bradley, R., Keimig, F., 2005. Stable isotopes in precipitation in the Asian monsoon region. *J. Geophys. Res.* 110, D23108.
- Williams, V.S., 1983. Present and former equilibrium-line altitudes near Mount Everest, Nepal and Tibet. *Arct. Alp. Res.* 15, 201–211.
- Wright, H.E., Mann, D.H., Glaser, P.H., 1984. Piston corers for peat and lake sediments. *Ecology* 65, 657–659.
- Xia, Zhong-Huan, Xu, Bai-Qing, Mugler, I., Wu, Guang-Jian, Gleixner, G., Sachse, D., Zhu, Li-Ping, 2008. Hydrogen isotope ratios of terrigenous *n*-alkanes in lacustrine surface sediment of the Tibetan Plateau record the precipitation signal. *Geochim. J.* 42 (4), 331.
- Xu, X., Lu, C., Shi, X., Gao, S., 2008. World water tower: an atmospheric perspective. *Geophys. Res. Lett.* 35, L20815.
- Zhang, J., Chen, F., Holmes, J.A., Li, H., Guo, X., Wang, J., Li, S., Lü, Y., Zhao, Y., Qiang, M., 2011. Holocene monsoon climate documented by oxygen and carbon isotopes from lake sediments and peat bogs in China: a review and synthesis. *Quat. Sci. Rev.* 30, 1973–1987.